nature geoscience

SUPPLEMENTARY INFORMATION

https://doi.org/10.1038/s41561-019-0453-0

In the format provided by the authors and unedited.

Dome formation on Ceres by solid-state flow analogous to terrestrial salt tectonics

M. T. Bland[1*], D. L. Buczkowski[2], H. G. Sizemore[3], A. I. Ermakov[4], S. D. King[5], M. M. Sori[6], C. A. Raymond[4], J. C. Castillo-Rogez[4] and C. T. Russell[7]

[1]US Geological Survey, Astrogeology Science Center, Flagstaff, AZ, USA. [2]Johns Hopkins Applied Physics Laboratory, Laurel, MD, USA. [3]Planetary Science Institute, Tucson, AZ, USA. [4]Jet Propulsion Laboratory, California Institute of Technology, Pasadena, CA, USA. [5]Virginia Tech, Blacksburg, VA, USA. [6]University of Arizona, Tucson, AZ, USA. [7]University of California, Los Angeles, Los Angeles, CA, USA. *e-mail: mbland@usgs.gov

Supplemental Material

Dome formation on Ceres by solid-state flow analogous to terrestrial salt tectonics

M. T. Bland[1,*], D. L. Buczkowski[2], H. G. Sizemore[3], A. I. Ermakov[4], S. D. King[5], M. M. Sori[6], C. A. Raymond[4], , J. C. Castillo-Rogez[4], C. T. Russell[7].

1. Gravitational differential loading and fluid flow

Gravitational differential loading is one of the primary drivers of salt tectonics on Earth. The mechanism can be simply conceptualized using the framework of hydraulic head [Kehle 1988; Hudec and Jackson 2007], in which fluids flow in response to a head gradient. A fluid's hydraulic head is the sum of the fluid's pressure and elevation head, so head gradients result from a combination of lateral differences in elevation head and pressure head (Fig. S1). The elevation head is the elevation (z) of a parcel of fluid above some reference level, and the pressure head is the height of the fluid column that could be supported by the weight of the overburden. The pressure head is

$$h_p = \frac{P}{\rho_i g} = \frac{\rho_c}{\rho_i} t,$$

where P is the lithostatic pressure and is given by $\rho_c g t$ with ρ_c the density of the crust, ρ_i the density of the fluid, g the gravitational acceleration, and t the thickness of the overburden. A lateral difference in the elevation of the fluid (Δz) or the thickness of the overburden Δt results in a lateral difference in hydraulic head

$$\Delta h = \Delta z + \left(\frac{\rho_c}{\rho_i}\right) \Delta t.$$

In the reference model shown in Fig. 2 (main text), gradients in both elevation head and pressure head exist. Fluid particles at the top of the column are higher than those in the layer below, which drives flow to the right side of the domain; however, the difference in overburden thickness is substantial and drives flow into the column. In this case, since the difference in elevation and overburden thickness are related ($\Delta z = -\Delta t$), the total difference in hydraulic head is

$$\Delta h_1 = \left(\frac{\rho_c}{\rho_i} - 1\right) \Delta t.$$

Here Δh_1 is the height to which the fluid column would rise in the limit of no resistance. Note that the same height can be derived using a simple isostatic approach. For our reference simulation, $\Delta h_1 = 3.1$ km, which represents the upper limit to which a dome could rise given the assumed geometry. In realty, the strength and flexural resistance of the overlying crust, and drag along the boundary between the crust and the low-viscosity, low-density (LVLD) material resists dome growth (Section 3), and our simulation results in a dome ~2 km high after 10 Myrs.

The above analysis demonstrates that the maximum dome height is primarily limited by the hydraulic gradients present in the subsurface (although dome width is also important, see main text and Section 5). That is, domes even larger than that in our reference simulation can be produced given a larger difference in overburden thickness (Section 5), or larger density contrasts (Section 4). An example is shown in Fig. S6a,b, in which a 1-km increase in Δt relative to the reference simulation produces a dome 3 km high.

Even larger differences in hydraulic head can be generated for a LVLD layer of uniform thickness beneath crater topography (case-2 simulations, Fig. 4 of main text). In this case no elevation head is present ($\Delta z = 0$) to acts against the pressure head, as occurred in case 1, and the total difference in hydraulic head is simply

$$\Delta h_2 = \frac{\rho_c}{\rho_i} \Delta t.$$

Note that for a given crater shape, changing the *depth* of the layer does not change the difference in hydraulic head, as Δt does not change. Instead, it is the depth of the crater (i.e., the difference between the crater rim and the crater floor) that controls the hydraulic head. Deep craters result in large Δt, whereas shallow craters result in small Δt. Dome formation is therefore more likely in larger, deep craters. For example, Duginavi crater, the host of Cosecha Tholus, is more than five kilometers deep when measured from its eastern rim. Increasing the layer depth does, however, increase the resistance of the overburden (as does decreasing the layer thickness), resulting in smaller domes even for the same Δh_2.

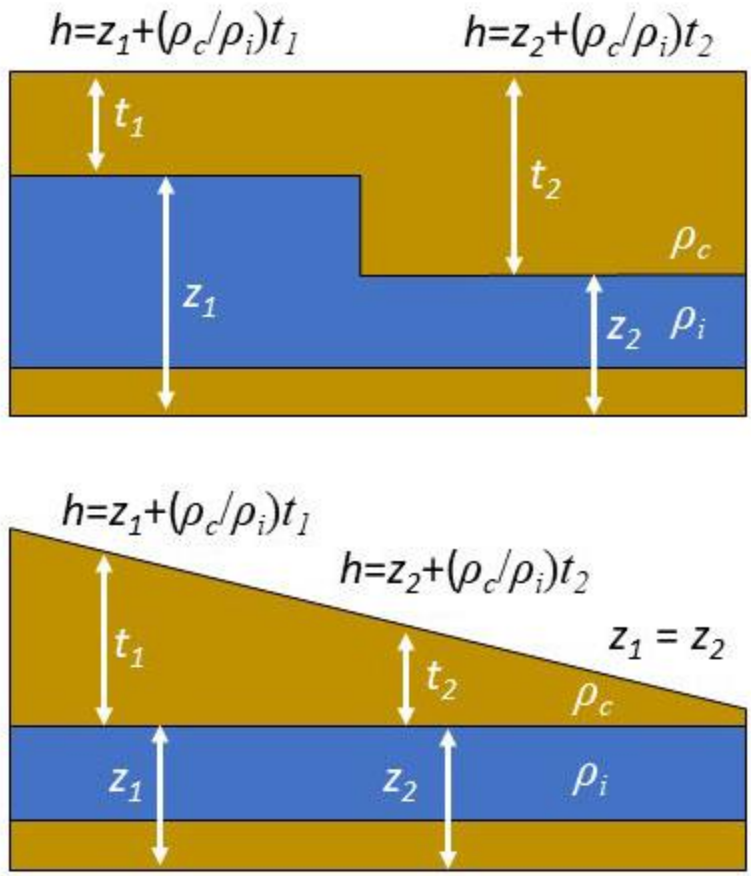

Figure S1: Illustration of subsurface geometries that result in hydraulic head gradients. The blue regions represent low-viscosity, low-density (LVLD) material and the brown regions represent the higher-viscosity, higher-density crust. **A**. Differential loading due to differences in LVLD layer thickness. The geometry is similar to that used in our case 1 simulations. **B.** Differential loading due to surface topography. The geometry is similar to that used in our case 2 simulations. After Hudec and Jackson [2007].

2. Gravity data

The presence of concentrated regions (e.g., lenses or layers) of low-density material in the crust, as assumed here, would create a mass deficit relative to "normal" crust and a negative gravity anomaly. Dawn gravity data, which is accurate to degree 16 [Ermakov et al. 2017; Konopliv et al. 2018], generally does not reveal the presence of mass anomalies associated with Ceres' domes. The exception is Ahuna Mons, which exhibits a positive anomaly indicating a mass excess [Ermakov et al. 2017; Ruesch et al. 2019b]. The absence of a gravity signature associated with low-density material at depth places some limits on the scale (and/or density contrast) of the buried low-density material. Figure S2 shows that the gravity anomaly associated with our case-1 subsurface geometry would likely be undetectable when truncated to degree 16, especially if other geologic features contribute to "noise" in the gravity data. The geometry needed to produce our case-1 domes is therefore consistent with currently available gravity data. The magnitude of the gravity anomaly is larger for larger deposits of low-density material. The threshold for detectability in the current gravity data is roughly a sphere 20 km in radius buried at 20 km depth (i.e., so that the top of the low-density material just touches the surface). The geometry assumed in our case-2 simulations approaches this limit, and might be detectable in the current data if it were present. Certainly, the extended sheet of low-density material shown in Figs. S11 and S13 would have a strong gravity signature (~200 mgal); however, this geometry was only used for simplicity, and as described in the main text (and below), a more laterally confined layer produces very similar dome formation results. We conclude that our hypothesis is generally consistent with current gravity data; however, additional analysis should be performed to determine whether solid-state flow is consistent with both the morphology of specific surface features and Dawn gravity data.

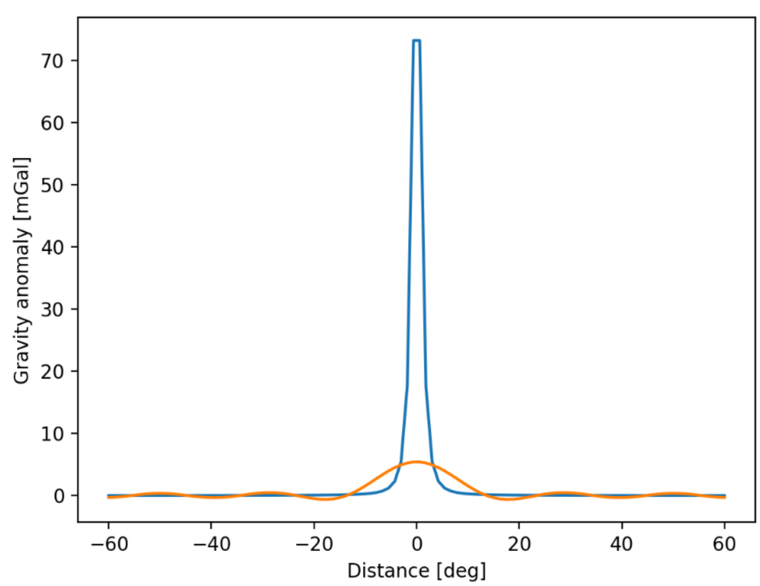

Figure S2: The gravity anomaly associated with a sphere of low density (920 kg m^{-3}) material 10 km in radius buried at a depth of 10 km (i.e., so that the top of the sphere just touches the surface). The blue curve shows the calculated anomaly, and the orange curve shows the anomaly expanded in spherical harmonics and truncated at degree 16. The ~5 mgal anomaly would not be detectable in the current gravity data.

3. Resistance to flow: drag and flexural rigidity

Flow of the low-viscosity, low-density material is resisted by at least two factors: drag (friction) along the boundary with the crustal material, and the strength of the encasing material. In our simulations, thicker or wider LVLD layers are less affected by drag because a smaller fraction of the LVLD material is in contact with the HVHD crust. This effect is observed in terrestrial salt tectonics [Hudec and Jackson, 2007] and illustrated in the simulations described above.

More important to our results is the strength of the overburden, and in particular, its resistance to flexure (i.e., the flexural rigidity). In general, the flexural response of the lithosphere depends on the wavelength (λ) of the load. For a periodic load, which our imposed geometry approximates, negligible lithospheric deformation occurs when

$$\lambda \ll 2\pi \left(\frac{D}{\rho_c g}\right)^{\frac{1}{4}},$$

where D is the flexural parameter given by

$$D = \frac{Et^3}{12(1-\upsilon^2)},$$

with E the Young's modulus, t the lithospheric thickness, and υ the Poisson's ratio. In contrast when

$$\lambda \gg 2\pi \left(\frac{D}{\rho_c g}\right)^{\frac{1}{4}},$$

the rigidity of the lithosphere is unimportant, and the solution approaches the isostatic case [see, e.g., Turcotte and Schubert 2002]. That is, for short wavelength topography the lithosphere is effectively infinitely ridged, and no deflection of the lithosphere occurs. Long wavelength topography, in contrast, is fully compensated (in hydrostatic equilibrium).

Flexural uplift of the lithosphere in our case-1 simulations can roughly be approximated as the loading of an elastic plate by a line load, for which the flexural half-wavelength is given by [Turcotte and Schubert 2002]

$$x_o = \frac{3\pi}{4}\alpha = \frac{3\pi}{4}\left(\frac{4D}{\rho_c g}\right)^{\frac{1}{4}}.$$

Figure S3 shows the flexural half-wavelength for a line load (solid curve) as well as the critical half wavelength for a periodic load (equations above, dashed curve) using identical parameter values to those in our simulations. Notably, in every simulation we performed, the width of the imposed load (i.e., the LVLD column width, blue bar in Fig. S3) is less than the flexural wavelength for the lithospheric thickness used (green box in Fig. S3). Our simulations are therefore far from the hydrostatic case (also represented by the maximum head gradient in Section 1) and the flexural rigidity of the lithosphere is important in resisting flow. The plot also helps to illustrate why the width of the LVLD column affects the results for our case-1 simulations. For a thickness (t) of 2 km (the overburden thickness directly above the column in our reference case-1 simulation) the flexural half-wavelength and critical wavelength are similar: ~39 km. In the reference simulation, the half-wavelength of the column is 10 km, four-times less than the critical value. Thus, deformation is strongly inhibited by the flexural resistance of the lithosphere. In contrast, when the half-width of the column is increased to 15 km the load wavelength is closer to the critical wavelength and resistance is reduced. A column significantly wider than 40 km would produce a dome with a height approaching the isostatic limit. For our simulation with a 5-km half-wavelength we approach the limit under which no deformation occurs: the lithosphere is extremely rigid. Further increasing the lithospheric thickness (such as in Figs. S7 and S11e,f) increases the flexural wavelength well beyond the wavelength of the simulated loads, and therefore results in negligible deformation.

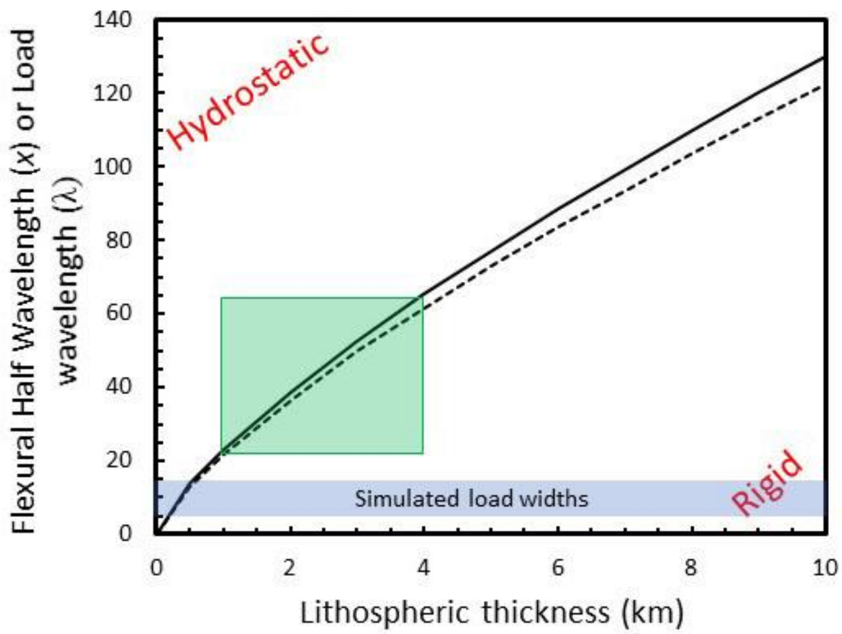

Figure S3: The flexural half wavelength for a line load on an elastic plate (black solid curve), and the critical wavelength for flexure (black dashed curve) using the lithospheric parameters assumed in our case-1 simulations. The blue bar shows load (i.e., column) widths used in our simulations, and the green box shows the range of half-wavelengths resulting from the typical lithospheric thicknesses used in our simulations. The infinitely rigid and hydrostatic limits are indicated.

4. The effect of viscosity and density on dome formation

For simplicity, and to more clearly illustrate the physics, the reference simulations shown in the main text (Fig. 2 and 4) and below (Figs. S6-S10) use end-member compositions: water ice for LVLD material (ρ = 920 kg m^{-3}) and a crustal density at the upper end of that permitted by Dawn gravity data [Ermakov et al. 2017], and with low-density volatile phases removed (i.e., 1400 kg m^{-3}). Additionally, we assume a discrete boundary between the layers. The situation on Ceres may be more complex, with the LVLD material consisting of a mix of ice-rock-salt, and the crust having a lower density. Boundaries between material types (e.g., LVLD and HVHD) may be gradational, with ice-content increasing across a finite-thickness boundary layer. In this work we seek to establish the plausibility of the solid-state mechanism for dome formation, and a full analysis of the complex behavior of compositionally mixed layers is beyond the scope of this focused study. However, we can evaluate the role of viscosity and density on dome formation, thus providing insight into how compositionally impure layers would behave.

To better understand the role of viscosity and density, we performed suites of simulations that varied the two material properties independently. In reality, the two properties may or may not be linked: adding silicate or salts to an ice layer will increase both its viscosity and its density, whereas adding clathrate will only increase its viscosity. In each simulation we assumed a geometry identical to the reference simulation for isolated dome formation (Fig. 2 of the main text), with a LVLD layer at a depth of 8 km, and a column of material rising to within 2 km of the surface. The difference in overburden thickness (Δt) is thus 6 km. The total width of the column was 20 km. Figure S4 shows dome growth as a function of time for four different LVLD material viscosities. The primary role of viscosity is to control the timescale of dome formation, rather than the ultimate height of the dome. For example, at the lowest viscosity shown, the dome reaches a height of 2 km in ~25 Myrs, whereas for a much higher viscosity a similar dome height is not reached until 1 Gyrs. Both simulations result in nearly identical structures, but the low-viscosity material permits domes to form faster. These numerical results are consistent with our analytical development in Section 1, which indicates that dome height is, to first order, independent of viscosity.

In contrast, the relative density of the LVLD and crustal materials does control the total dome height. Figure S5 shows the height of the dome after 10 Myrs for four different density ratios (ρ_i / ρ_c), including the ratio used in our reference simulation (0.66). Unsurprisingly, our simulations confirm that dome height has a linear relationship with density gradient, consistent with the discussion in Section 1 above. Interestingly, the strength of the crust causes dome height to go to zero at $\rho_i / \rho_c \approx 0.9$, rather than 1, as our simplified analytical development would predict.

These simulations indicate that forming domes by a salt tectonics-like mechanism may require lenses or layers of relatively pure ice in the subsurface. The higher viscosity of a mixed ice-particulate layer only affects the formation timescale and is not an impediment to dome formation. However, although domes are not driven by a Rayleigh-Taylor instability (a difference in elevation or overburden thickness is required), a strong density contrast is required for dome formation. Achieving a sufficient density contrast is more challenging without relatively pure ice.

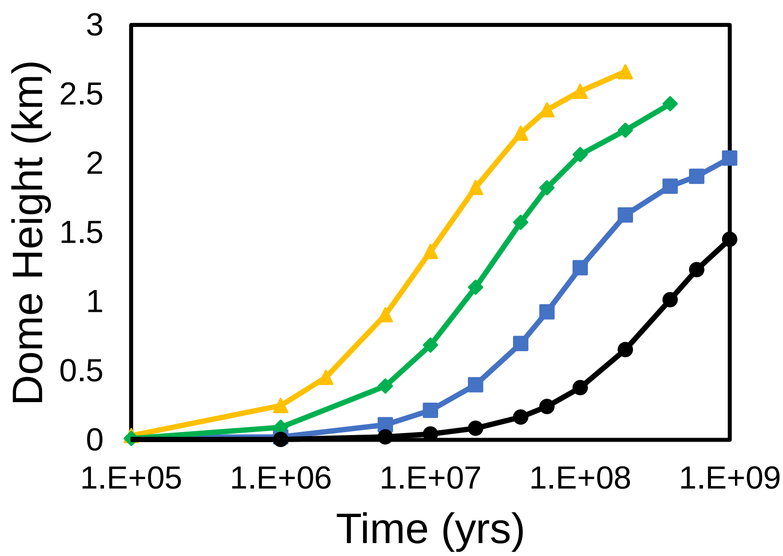

Figure S4: Dome growth as a function of time for four simulations that used different viscosities for the LVLD layer (yellow is lowest, black is highest). Each case used the same initial geometry: a layer buried 8 km deep and a central column rising to within 2 km of the surface. All of the viscosities used were higher than that in our reference simulation (Fig. 2).

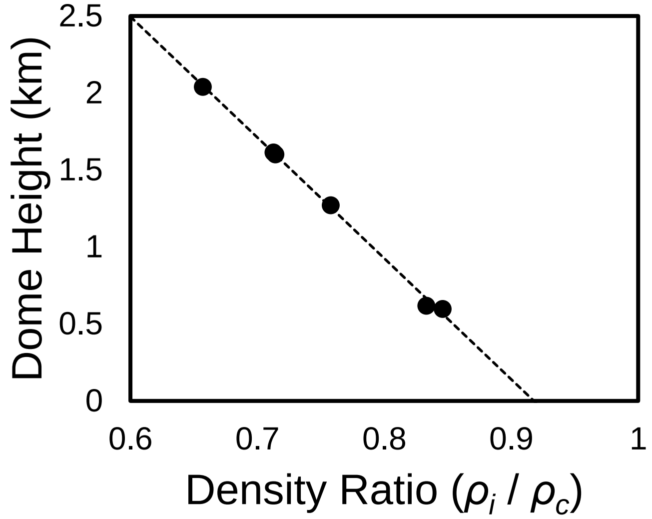

Figure S5: Dome height after 10 Myrs as a function of the ratio of densities. Black points are simulation output, the dashed line is a linear fit to the data. The point at $\rho_i / \rho_c = 0.66$ is the reference simulation (Fig. 2). Although not driven by a Rayleigh-Taylor instability, a significant density contrast is required for dome formation.

5. Dependence of dome formation on subsurface layer geometry: Case 1.

Figures S6-S10 show simulation results for variations in subsurface LVLD layer geometry. Each “final” simulation is shown after 10 Myrs (with one exception: Fig. S9f), which provides sufficient time for the domes to approach their maximum height (Fig. 3 of main text). In a few cases, dome growth would likely continue past 10 Myrs; however, domes will never exceed the height defined by the difference in hydraulic head (indicated).

As described in Section 1, dome height depends strongly on the hydraulic head gradient; however, the resistance of the overburden, the width of the subsurface column, and the width of the layer all affect dome growth (section 3). Figure S6 shows simulations with geometries that include relatively large Δh_1, and subsequently develop large domes. The largest (Fig. S6a,b) is nearly 3 km tall. Figure S6c,d is the reference simulation described in the main text. Figure S6e,f shows an interesting case in which Δh_1 is identical to that in Fig. S6a,b, but the thicker overburden and the thinner adjacent layer produce more resistances to dome growth via flexural resistance, drag, and volumetric constraints. The result is a dome similar in amplitude to the reference simulation. Comparison of Fig. S6g,f and Fig. S6c,d (the reference) clearly demonstrates the importance of hydraulic head. The former simulation includes less drag and the same flexural resistance; however, the smaller head yields a dome just 1.5 km tall.

Figure S7 shows simulations with subsurface geometries that yield relatively small lateral differences in hydraulic head. The geometry in Fig. S7a,b includes substantial LVLD material in the near surface; however, the magnitude of the differential loading is small, resulting in only a 760 m upwarping of the surface. The Δh_1 in the simulation shown in Fig. S7c,d is larger than that in Fig. S6e,f, but the thicker crust above the column resists upward flow, and the resulting dome is only 930 m high. The deeply buried LVLD material in the simulation shown in Fig. S7e,f produces essentially no surface deformation despite having Δh_1 greater than that shown in Fig.

S7a,b. Although the surface deflections produced by the simulations shown in Fig. S7 are small, similar geometries on Ceres would contribute to the “lumpy” surface morphology observed on parts of the body.

Figure S8 clearly shows the dependence of final dome height on the width of the LVLD column of material. Each simulation has the same Δh_1; only the width of the column was changed. A 10-km wide column (Fig. S8a,b) produces just 250 m of surface deflection. The reference simulation (shown again for comparison in Fig. S8c,d) is 20-km wide and yields a 2 km high dome. A 30-km wide column yields a dome 2.5 km high. Thus, one might not expect domes smaller than ~10-20 km to form by differential loading on Ceres (see Section 3). Indeed, Sizemore et al. [2019] suggests that most domes have diameters of 30-120 km, consistent with their formation through solid-state flow.

Additional simulations including wide columns at depth are shown in Fig. S9. When Δh_1 is small and the overburden is thin (Fig. S9a,b), differential loading can produce a broad, flat-topped platform 900-950 m above its surroundings. A large Δh_1 produces a dome 2.4 km high (Fig. S9e,f) after just 6 Myrs. In this simulation, lateral flow is limited by drag in the relatively narrow layer at depth, as well as volumetric constraints.

Finally, Fig. S10 shows how the vertical and lateral extent of the LVLD layer affects simulation results. Each simulation shown has the same Δh_1, and Fig. S10a,b is the reference simulation for comparison. A laterally restricted layer (Fig. S10c,d) limits dome growth, producing a dome 1.5 km high. In this case the rise of the dome is limited by the volume of LVLD material available to flow. Here we may also see a limitation of our Lagrangian finite element approach to simulating salt tectonics. Flow in the layer appears to be restricted by the vertical boundary in the high-viscosity material. As noted previously, flow in a thin layer (Fig. S10e,f) is also restricted by drag at the boundary with the surrounding crust. Boundary drag is common in terrestrial salt tectonics [Hudec and Jackson, 2007].

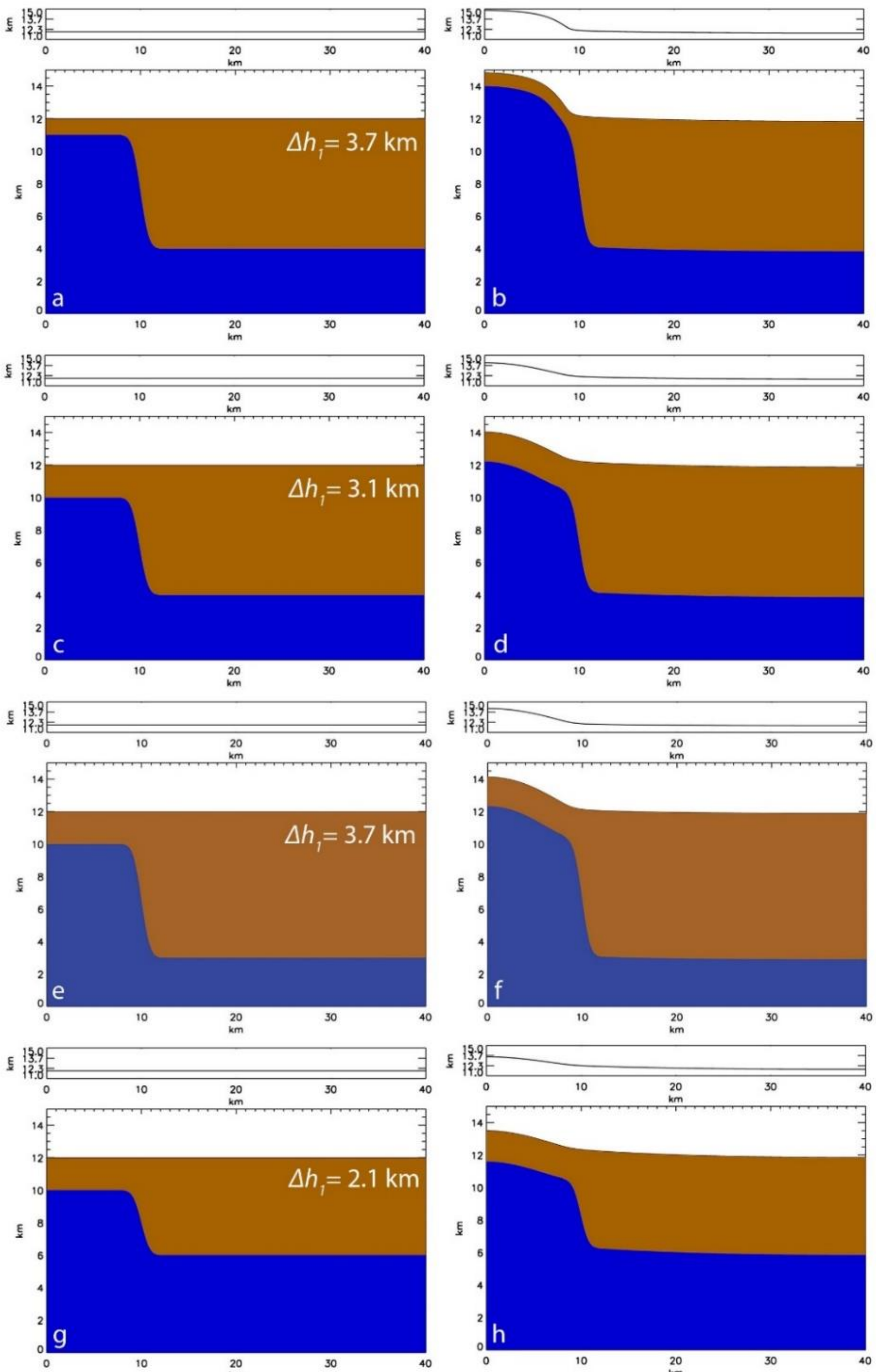

Figure S6: Case 1 simulations with layer geometries that include relatively large Δh_1, and subsequently develop large domes. In each pair (a,b; c,d; e,f; g,h) the initial geometry is shown at left with the Δh_1 indicated. The surface and subsurface deformation after 10 Myr is shown at right. The reference case-1 simulation (shown and described in the main text) is shown in panels c,d. The LVLD layer is shown in blue and the higher viscosity and density crust is shown in brown.

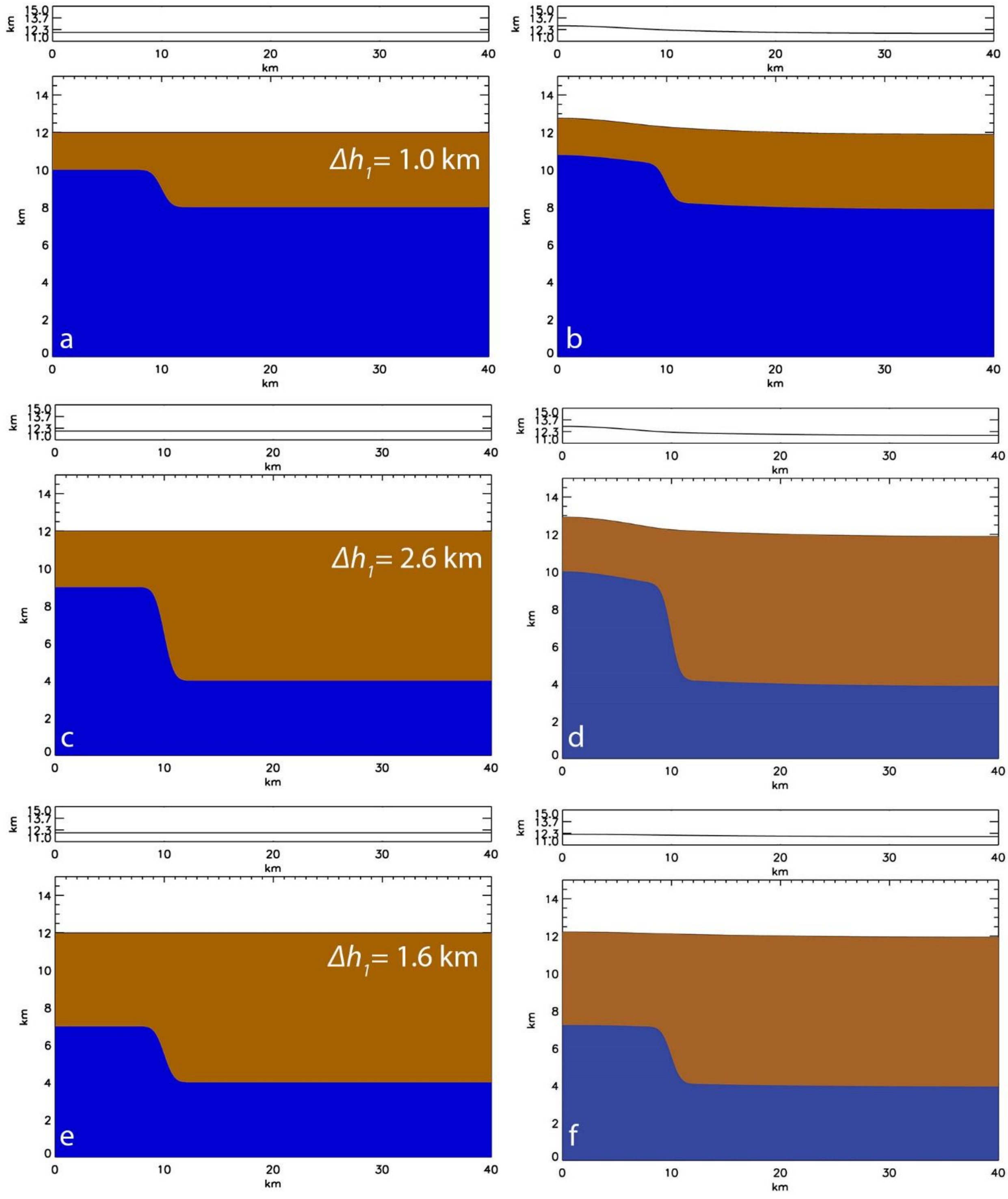

Figure S7: Case-1 simulations with layer geometries that include relatively small Δh_1, and subsequently develop small domes. In each pair (a,b; c,d; e,f) the initial geometry is shown at left with the Δh_1 indicated. The surface and subsurface deformation after 10 Myr is shown at right. The LVLD layer is shown in blue and the higher viscosity and density crust is shown in brown.

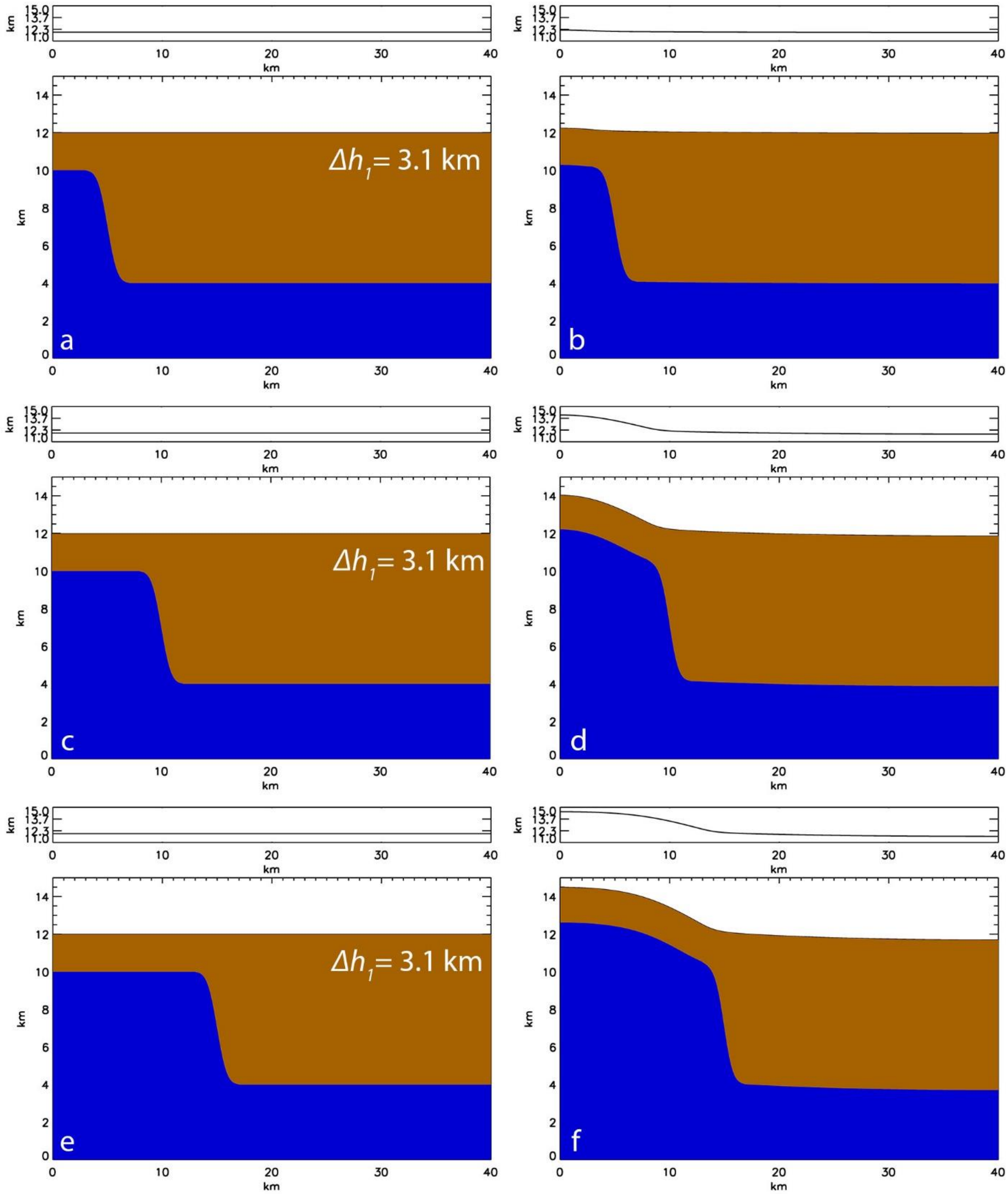

Figure S8: Case-1 simulations demonstrating the influence of subsurface column width. In each pair (a,b; c,d; e,f) the initial geometry is shown at left with the Δh_1 indicated. The surface and subsurface deformation after 10 Myr is shown at right. The simulations are axisymmetric so the full-width half-max of each column is 10 km, 20 km, and 30 km, respectively. The reference case-1 simulation (shown and described in the main text) is shown in panels c,d. The LVLD layer is shown in blue and the higher viscosity and density crust is shown in brown.

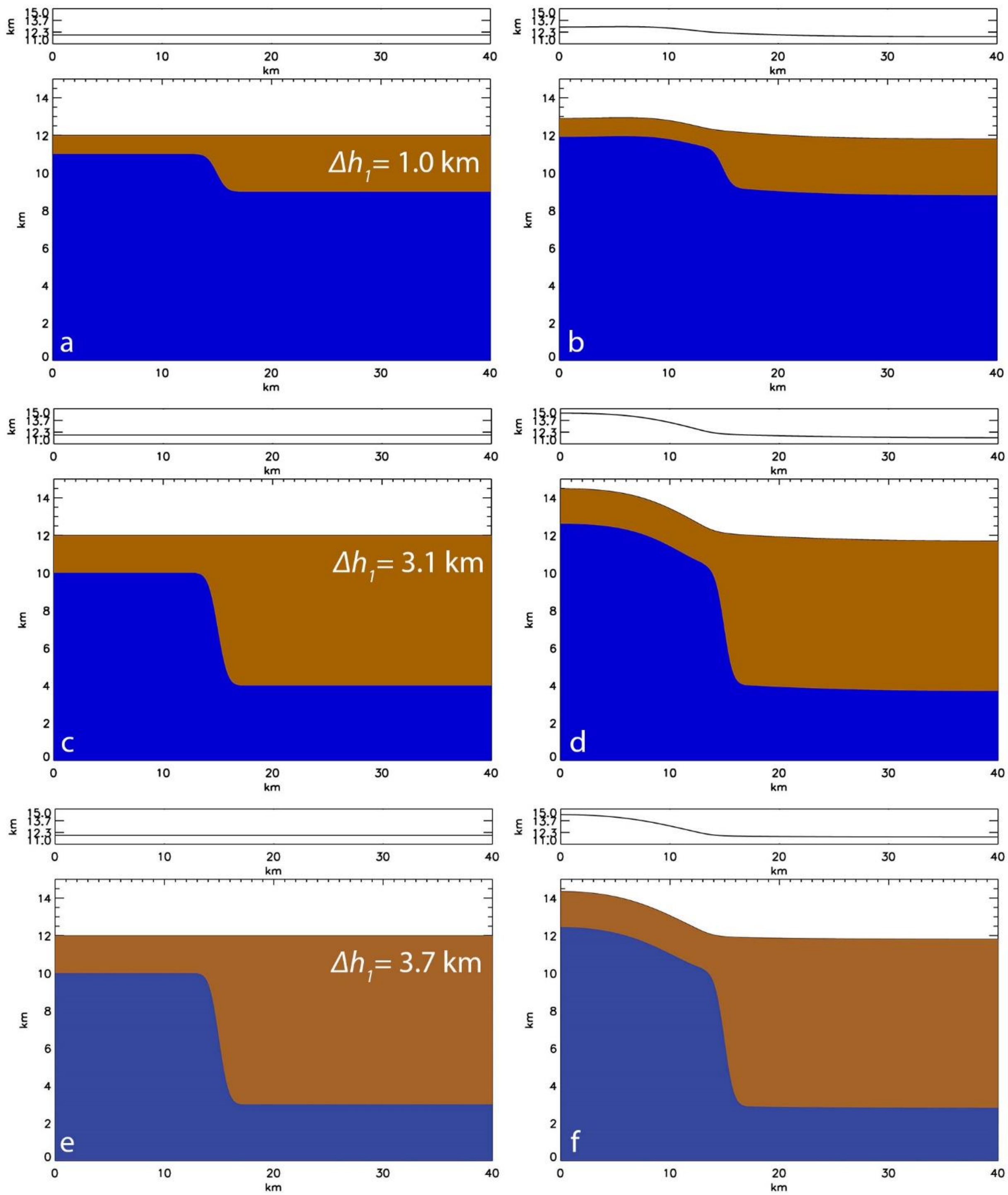

Figure S9: Case-1 simulations that used a wider subsurface LVLD column. In each pair (a,b; c,d; e,f) the initial geometry is shown at left with the Δh_1 indicated. The surface and subsurface deformation after 10 Myr is shown at right. The LVLD layer is shown in blue and the higher viscosity and density crust is shown in brown.

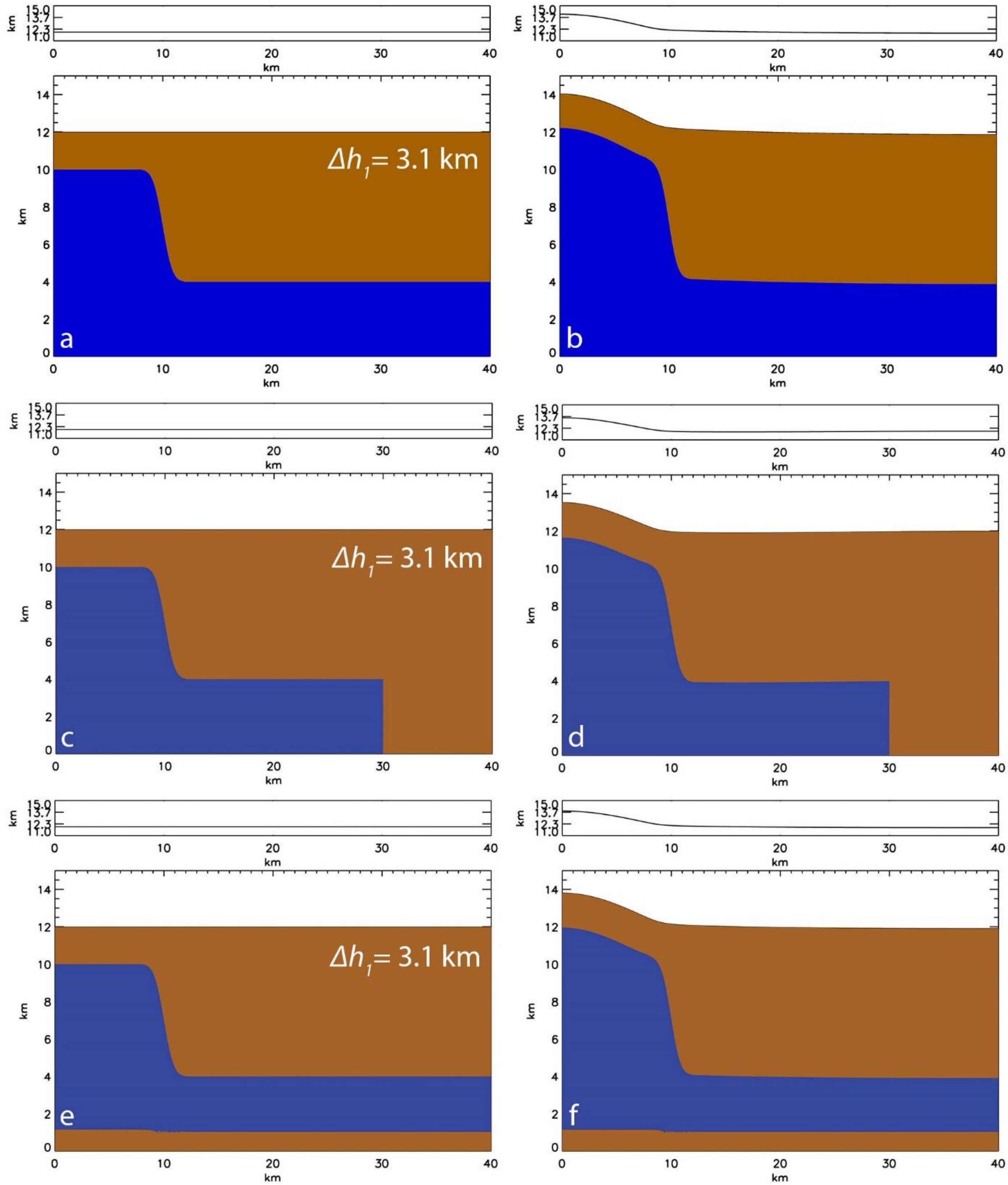

Figure S10: Case-1 simulations that shows how the vertical and lateral extent of the LVLD layer affects simulation results. Each simulation shown has the same Δh_1, and panel a,b is the reference simulation (shown and described in the main text) for comparison. In each pair (a,b; c,d; e,f) the initial geometry is shown at left with the Δh_1 indicated. The surface and subsurface deformation after 10 Myr is shown at right. The LVLD layer is shown in blue and the higher viscosity and density crust is shown in brown.

6. Dome formation driven by topographic differential loading: Case 2 simulations.

Figure S11 shows the results from simulations of differential loading induced by crater topography (our "case 2"). Each "final" simulation is shown after 0.8 Myrs. Dome growth is expected to continue beyond the end of the simulation shown; however, numerical limitations (specifically the lack of remeshing during large deformation) currently prevents us from extending the simulation. Because of the lack of axial symmetry, the simulations were performed in plane strain, as described in the methods section. In contrast to the case-2 reference simulation (Fig. 4), these simulations used a more laterally extensive layer of LVLD material. However, as noted below, the lateral extent has little effect on the results as long as there is sufficient LVLD material to form the dome, and the material is positioned beneath the crater rim.

Figure S11 shows four simulations that vary the lateral position, depth, and thickness of a partial layer of LVLD material beneath the crater. Figure S11a,b shows a simulation nearly identical to our case-2 reference simulation (Fig. 4), but with a LVLD layer that extends horizontally to the crater center, rather than just beyond the crater rim. As in our reference case, the layer is 10 km thick and at a depth of 5 km. The resulting "dome" is lower in amplitude than in the reference simulation, and has a flat or concave upper surface. Although the differential loading is identical to the reference case, the increased horizontal extent of the LVLD layer permits increased lateral flow and reduced vertical flow, relative to the reference. The resulting morphology is similar to that of Lughnasa Tholus in Bagbalel crater (Fig. S12), which is closer to the crater center and lower in amplitude compared to Cosecha Tholus, and includes a depression on the upper surface.

Figure S11c,d uses the same geometry as the reference simulation (Fig. 4) but the LVLD material extends to the edge of the domain (as in all of the simulations shown here). Both the simulation shown in Fig. S11c,d and the reference simulation in Fig. 4 produce a large dome that rises 3.6 km above the floor of the crater. The simulation demonstrates that the lateral extent of the layer beyond the crater rim does not affect the results.

Figures S11e,f and S11g,h show cases that produce smaller domes, or no surface deformation at all. Figure S11e,f includes a 10-km thick LVLD layer at a depth of 10 km: twice as deep as the reference simulation. The result shows minimal deflection of the crater floor. Figure S11g,h shows a simulation in which the layer is at a depth of 5 km, but is only 5-km thick. The resulting dome is similar to, but much smaller than, that in the reference simulation. The results of these simulations demonstrate the importance of factors that resist flow (Section 3). Both gradients in hydraulic head are identical to the reference simulation (Fig. S11c,d and see Section 1); however, flow of the deep layer is strongly resisted by the thicker overburden, and flow in the thin layer is constrained by volumetric limitations and drag along the layer edges (Section 3).

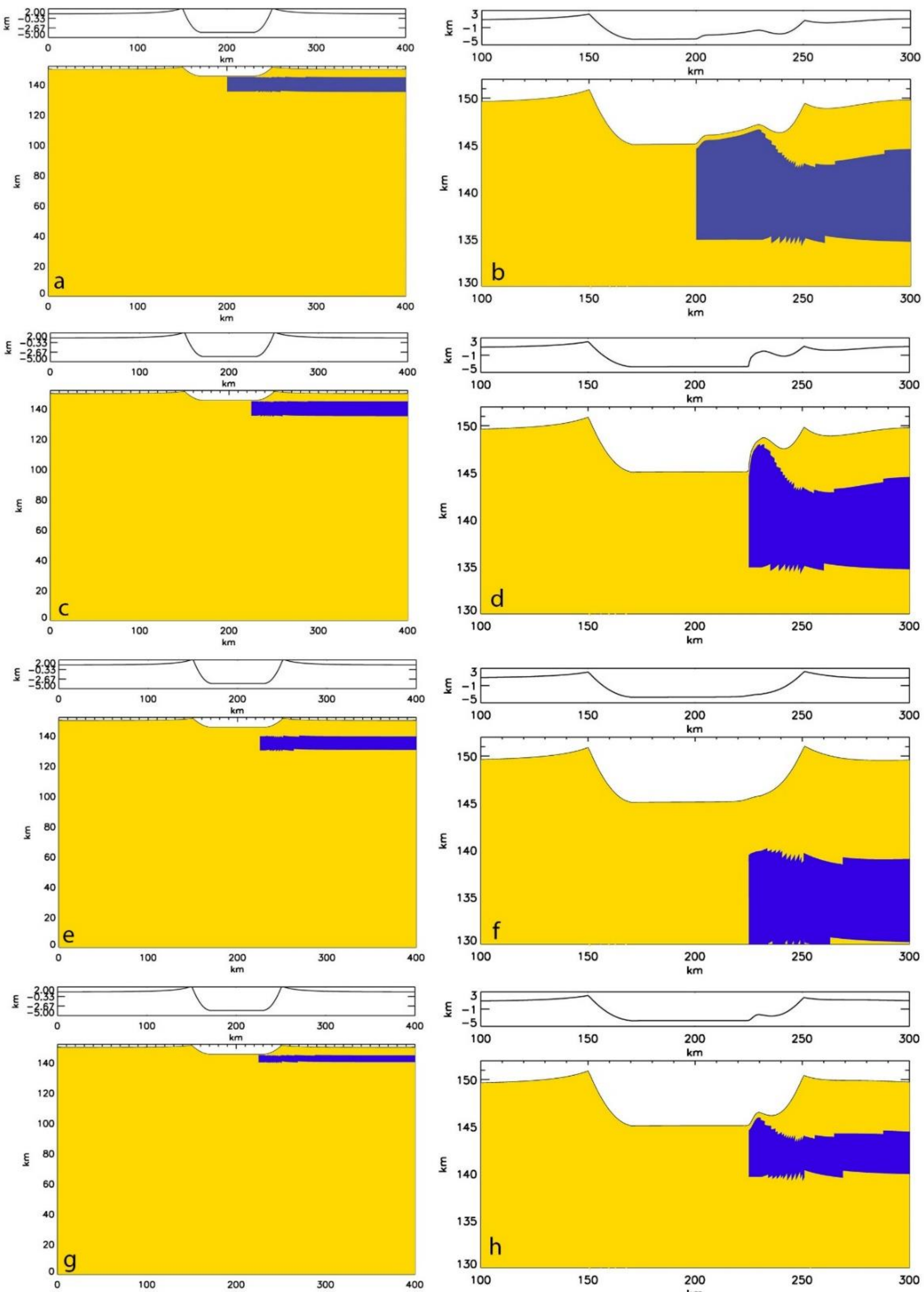

Figure S11: Case-2 simulations that illustrate the effect of differential loading driven by topography. In each pair (a,b; c,d; e,f; g,h) the initial geometry is shown at left and the surface and subsurface deformation after 0.8 Myr is shown at right (b,d,f,h). The LVLD layer is shown in blue and the higher viscosity and density crust is shown in yellow. Simulation a,b is similar to the reference simulation (shown in c,d) except the LVLD layer extends to the center of the crater. The simulation shown in e,f uses a 10 km thick layer at 10 km depth. The simulation shown in g,f uses a 5 km thick layer at 5 km depth.

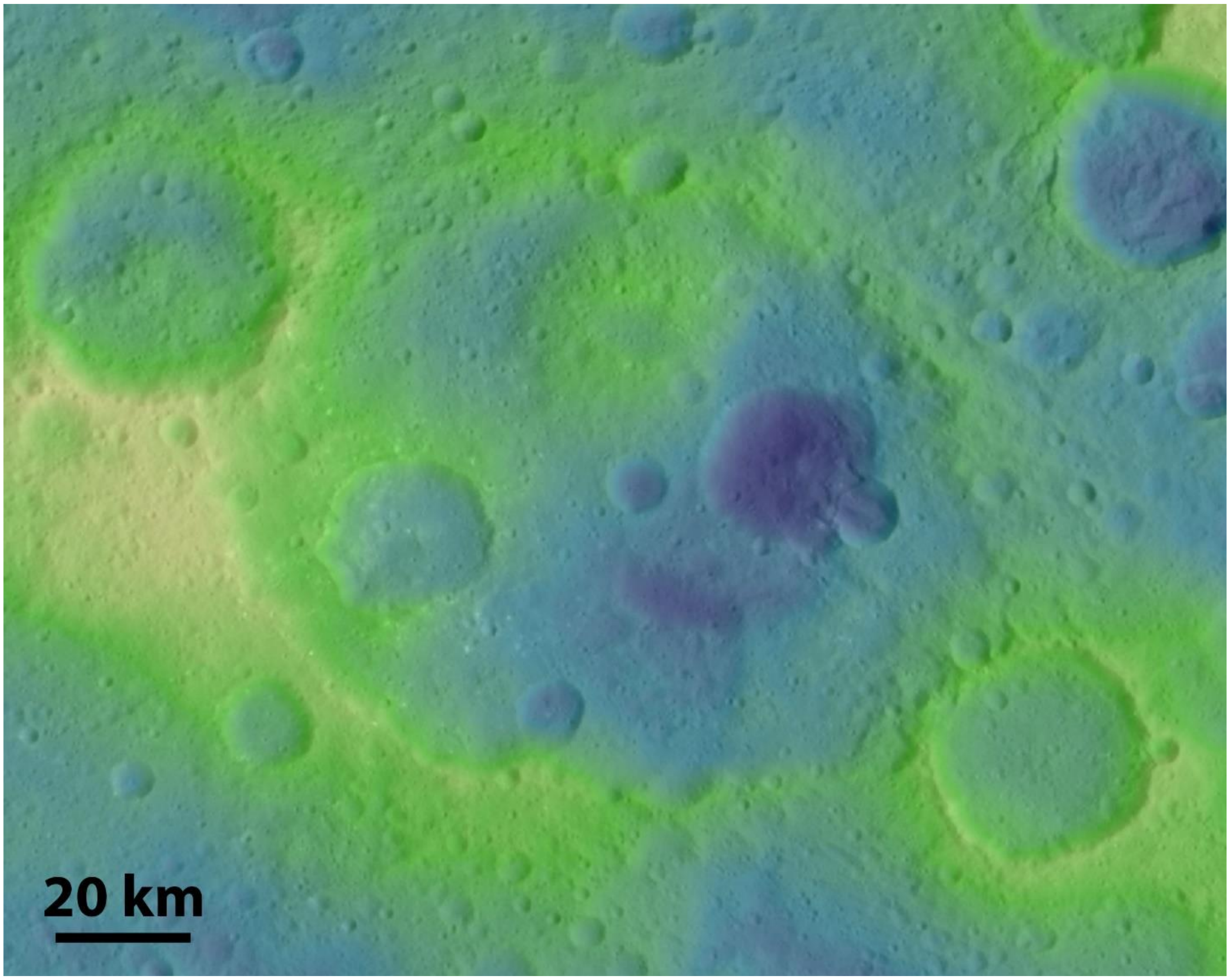

Figure S12: Begbalel crater with the prominent dome Lughnasa Tholus inside its northern rim. The dome rises 2-3 km above the floor of the crater. The structure, which includes a central depression is qualitatively similar to that shown in Fig. S11b.

7. Floor fractured craters created by solid-state flow

Figure S13 shows the results of two simulations that include a LVLD layer that extends beneath the entire crater. The two differ only in the horizontal extent of the layer, and produce nearly identical results. In both cases, the differential loading induced by the crater topography drives uplift of the entire crater floor (Fig. S14) and small-scale doming at the base of the crater walls. In this simulation the floor is uplifted by 230 m at the crater center, and the domes stand more than 1 km above the crater floor. Buczkowski et al. [2018] described numerous floor-fractured craters on Ceres, some of which include domes near the base of the crater wall (Fig. S15). By analogy with lunar floor fractured craters, Buczkowski et al. [2018] argued that the floor fractures result from uplift of the crater floor due to either (cryo)magmatic intrusion similar to laccolith formation, or solid-state flow. The simulations shown here support the solid-state flow hypothesis for floor-fractured craters.

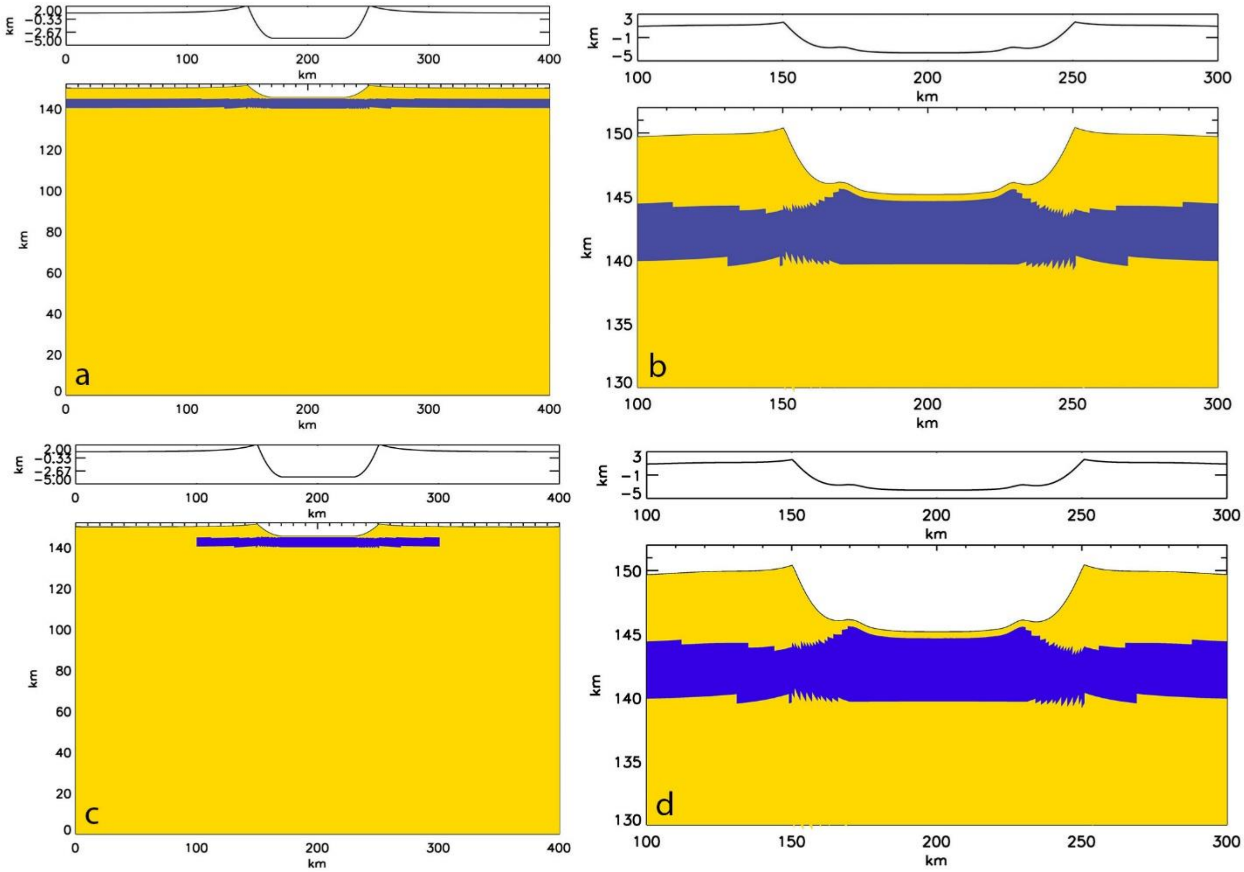

Figure S13: Simulation of differential loading positing a LVLD layer beneath the entire crater. The simulations both use a 10 km thick layer positioned 5 km beneath the surface (and just 500 m beneath the crater floor). The only difference between them is the lateral extent of the layer. In each pair (a,b; c,d) the initial geometry is shown at left (a,c) and the surface and subsurface deformation after 0.8 Myr is shown at right (b,d). The LVLD layer is shown in blue and the higher viscosity and density crust is shown in yellow. The simulations produce uplift of the crater floor consistent with floor-fractured craters.

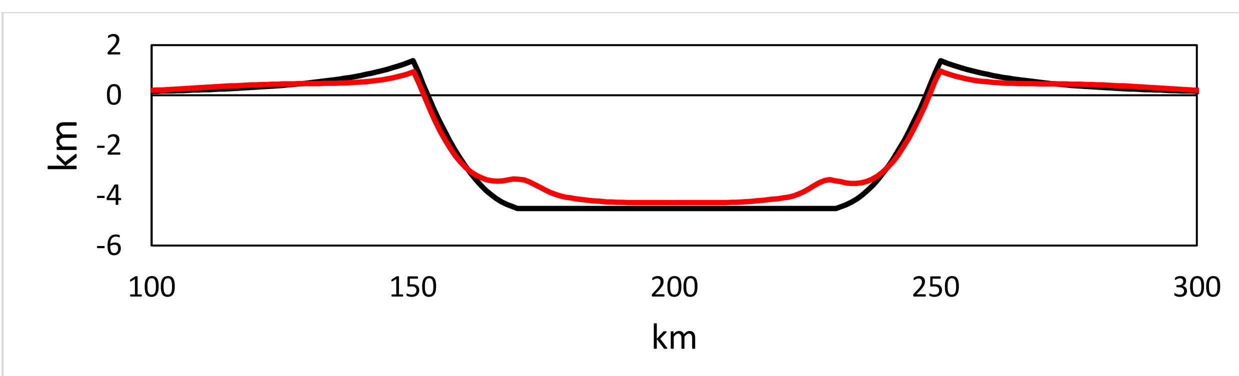

Figure S14: Profiles of the initial (black) and final (red) surface of a simulation that resulted in 230 m of crater floor uplift. The simulation is identical to that shown in Fig. S13c,d.

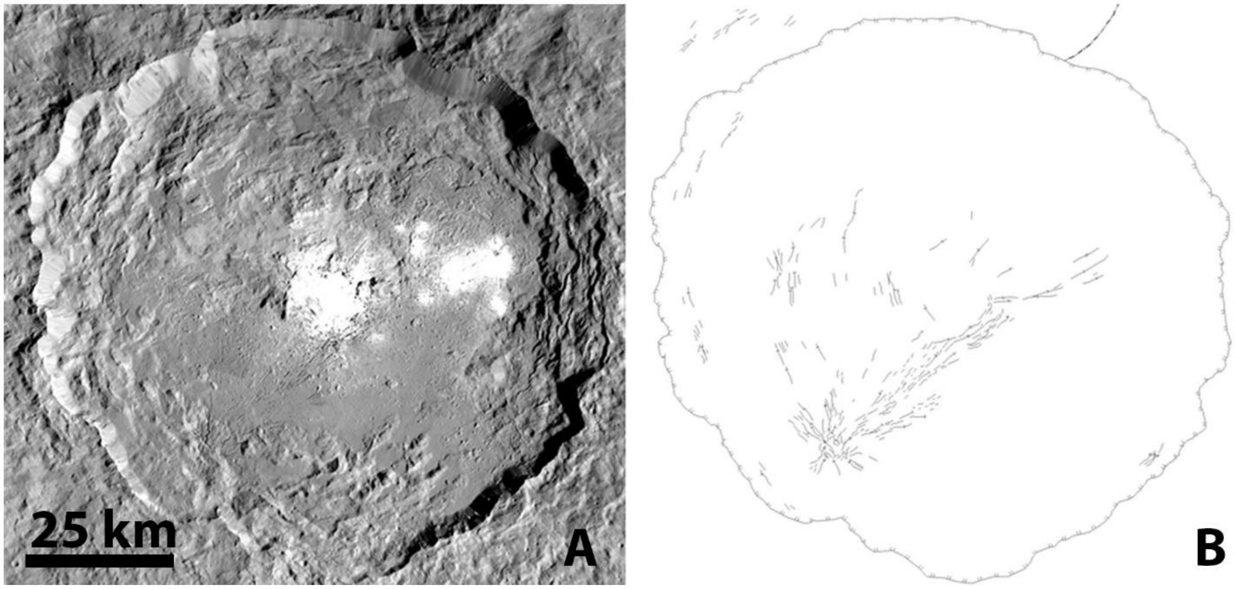

Figure S15: Floor fractures, possibly resulting from uplift of the crater floor [Buczkowski et al. 2018], are observed in numerous large craters on Ceres. A. Dawn Framing Camera image mosaic of Occator, a floor-fractured crater. **B.** Map of floor fractures within Occator from Buczkowski et al. [2018].

8. Forming Ahuna Mons-like structures by solid-state flow

The reference simulations shown in Fig. 2 of the main text and Figs. S6-S10 above are meant to describe the formation of typical large domes observed on Ceres. Most geometries result in structures a few kilometers tall and tens of kilometers in diameter. Ceres' Ahuna Mons, in contrast is 4 km tall, and roughly 17 km across, giving it a distinctively high aspect ratio. This unusual aspect ratio was used as the primary evidence for an extrusive cryovolcanic formation by Ruesch et al. [2016]: observations of terrestrial dacitic (felsic) domes can have similar ratios (we note that other geologic structures, such as pingos, and erosional buttes and mesas, can have similar aspect ratios). The solid-state flow mechanism proposed here can also produce high aspect ratio domes. Figure S16 shows one example. In this case, a thin overburden and large hydraulic head gradient results in a dome 3.27 km high after 10 Ma and 20 km in diameter. Although the dome resulting from this simulation is modestly shorter than Ahuna Mons, there is no physical reason why even larger domes cannot be formed from even larger hydraulic head gradients (say due to a more deeply buried layer, and thus thicker overburden) if such gradients exist. The only question is whether invoking such large gradients is plausible. The rarity of structures like Ahuna Mons may speak to the challenge of maintaining such large hydraulic gradients.

We also note that Ahuna Mons is morphologically distinct from most of Ceres' domes. As described in Ruesch et al. [2016], the summit morphology of Ahuna Mons consists of troughs and ridges without systematic orientation. Similar morphologies are not observed at other domes on Ceres (see Sizemore et al. [2019] and Fig. S17). In fact, most of Ceres' domes are difficult to identify morphologically – only their topographic expression gives them away. This is clearly not the case with Ahuna Mons. We therefore argue that Ahuna Mons is morphologically distinct from Ceres' other large domes, and might therefore have a different origin.

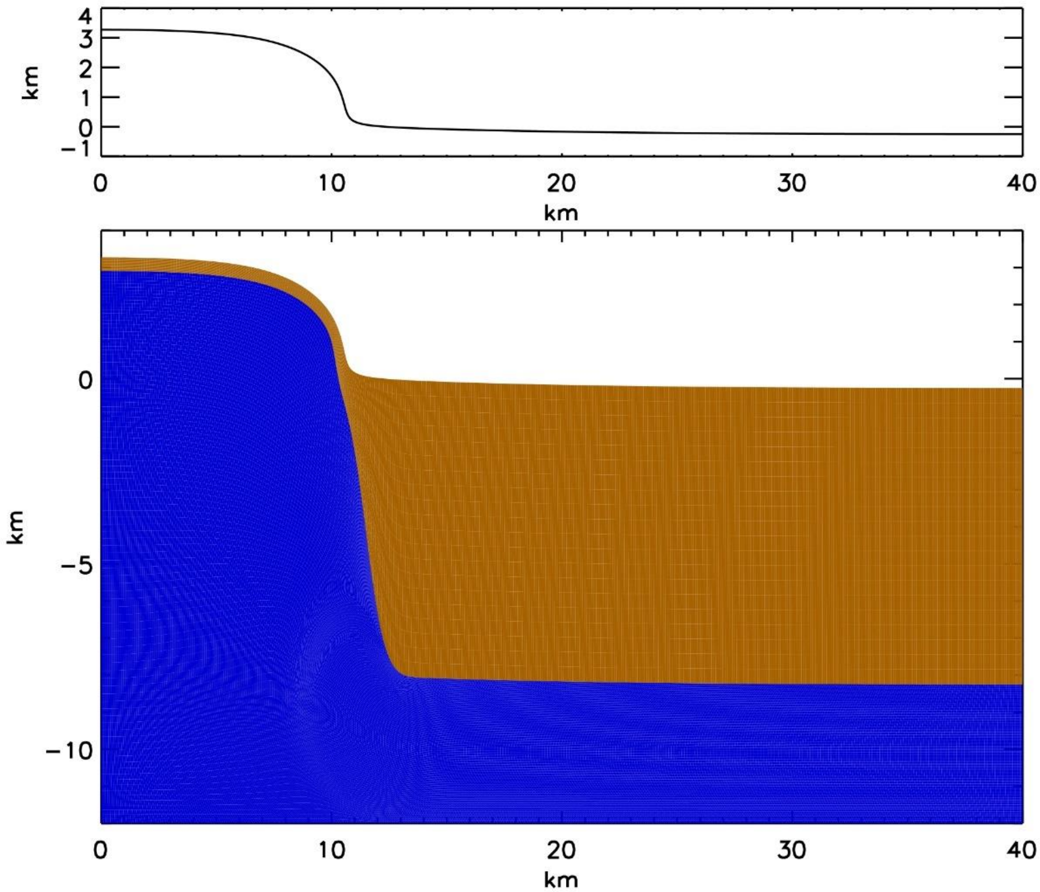

Figure S16: An example of an Ahuna Mons-like dome formed by salt tectonic-like deformation. The dome is 3.25 km high and 20 km in diameter: an aspect ratio approaching that of Ahuna Mons. The simulation was initialized with a very thin overburden (500 m) above the central column.

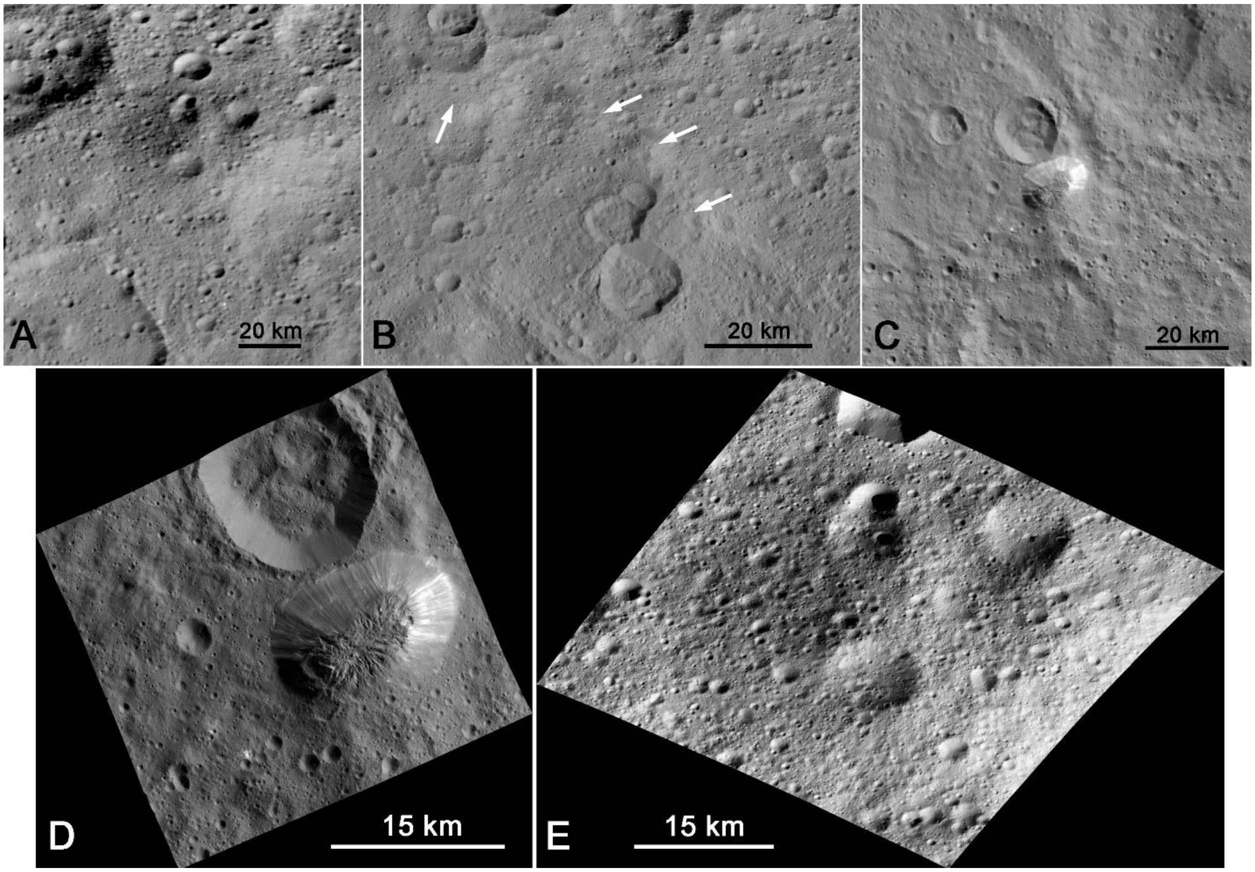

Figure S17: Comparison of "typical" dome morphologies (a, b, e) with that of Ahuna Mons (c, d). A. Hosil Tholus (center). B. Kwanzaa Tholus (white arrow at upper left) and Aymuray Tholi (three white arrows at right). C. Ahuna Mons. Panels A-C are from a Dawn image mosaic at 140 m/pixel. Note that domes are difficult to identify based on morphology alone. Ahuna Mons is the exception. D. Higher resolution (34 m/pixel) image of Ahuna Mons illustrating summit morphology. E. Higher resolution (36 m/pixel) images of Hosil Tholus illustrating lack of summit morphology. Note that Hosil Tholus is 3.5 km tall, modestly shorter than Ahuna Mons (but similar to the dome shown in Fig. S16). Panels D and E clearly show strong morphological differences between Ahuna Mons and typical domes.

References:

Buczkowski, D. L. *et al.* Floor-fractured craters on Ceres and implications for interior processes. *J. Geophys. Res.* (2018). https://doi.org/10.1029/2018JE005632

Ermakov, A. I., *et al.* Constraints on Ceres' internal structure and evolution from its shape and gravity measured by the Dawn spacecraft. *J. Geophys. Res.,* 122, 1-27 (2017). https://doi.org/10.1002.2017JE005302

Hudek, M. R., Jackson, M. P. A. Terra infirma: Understanding salt tectonics. Earth Sci. Rev. 82, 1-28 (2007). https://doi.org/10.1016/j.earscirev.2007.01.001.

Kehle, R. O. The origin of salt structures. In: Schreiber, B. C., Evaporites and Hydrocarbons. Columbia University Press, New York. pp. 345-404 (1988).

Konopliv, A. S. *et al*. The Ceres gravity field, spin pole, rotation period and orbit from the Dawn radiometric tracking and optical data. *Icarus* 299, 411-429 (2018). https://doi.org/10.1016/j.icarus.2017.08.005

Ruesch, O. *et al*. Slurry extrusion on Ceres from a convective mud-bearing mantle. Nat. Geo. 12, 505-509. https://doi.org/10.1038/s41561-019-0378-7

Sizemore, H. G. et al. A global inventory of ice-related morphological features on dwarf planet Ceres: Implications for the evolution and current state of the cryosphere. J. Geophys. Res. (2019). https://doi.org/10.1029/2018JE005699

Turcotte, D. L. & Schubert, G. Geodynamics (2nd Ed). Cambridge University Press, Cambridge (2002).